



“Double-punch” strategy against triple-negative breast cancer via a synergistic therapy of magneto-mechanical force enhancing NIR-II hypothermal ablation

Hui Du^{a,1}, Fang Yang^{a,b,**,1}, Chenyang Yao^a, Wenhao Lv^a, Hao Peng^a, Stefan G. Stanciu^c, Harald A. Stenmark^{d,e}, Young Min Song^f, Bo Jiang^a, Aiguo Wu^{a,b,*}

^a Cixi Institute of Biomedical Engineering, International Cooperation Base of Biomedical Materials Technology and Application, Chinese Academy of Sciences (CAS) Key Laboratory of Magnetic Materials and Devices, Zhejiang Engineering Research Center for Biomedical Materials, Ningbo Institute of Materials Technology and Engineering, CAS, Ningbo, 315201, China

^b Advanced Energy Science and Technology Guangdong Laboratory, Huizhou, 516000, China

^c Center for Microscopy-Microanalysis and Information Processing, University Politehnica of Bucharest, Bucharest, 060042, Romania

^d Center for Cancer Cell Reprogramming, Faculty of Medicine, University of Oslo, Montebello, N-0379, Oslo, Norway

^e Department of Molecular Cell Biology, Institute for Cancer Research, Oslo University Hospital, Montebello, N-0379, Oslo, Norway

^f School of Electrical Engineering and Computer Science, Gwangju Institute of Science and Technology, Gwangju, 61005, Republic of Korea

ARTICLE INFO

Keywords:

Triple-negative breast cancer
Magnetic nanoparticles
Magneto-mechanical force
Photothermal therapy
Cancer therapy

ABSTRACT

Triple-negative breast cancer (TNBC) is a form of breast cancer that is more aggressive and harder to treat than others, with a higher probability of relapse. Its nefarious capabilities for migrating and invading other parts of the body together with the current lack of clinically established effective therapies account for a low survival rate. In this work, we demonstrate the in-tandem use of two complementary therapeutic routes to effectively combat TNBC. A versatile magnetic-photothermal converter (MPC) consisting of zinc-doped ferrite nanoparticles and polyethylene glycol, is shown to display excellent therapeutic efficiency, being capable to fight TNBC via two distinct routes: magneto-mechanical force (MMF) and near-infrared-II (NIR-II) hypothermal ablation. The combined use of these two complementary and synergistic therapies, which are less aggressive to the human body compared to conventional chemotherapeutic approaches, results in the splendid suppression of TNBC migration and invasion. Remotely controlling the MPCs by an external magnetic field, results in cellular MMF effects that cause direct mechanical destruction to the cancer cell membrane, leading to its necrosis. Furthermore, the MMF disrupts intracellular lysosomes, thereby triggering the release of large amounts of protein hydrolases, which induce intracellular oxidative stress, and accelerate the induction of apoptosis. Complementing the therapeutic approach based on MMF, the excellent photothermal performance of the MPC in the NIR-II region (1064 nm) is exploited to enable effective hypothermal ablation of the tumours, which can be achieved in deep tissue layers. The proposed multifunctional nanocomposites, together with the demonstrated “double-punch” therapeutic approach, hold significant potential to pave the way for future cutting-edge weapons against the dreadful TNBC.

* Corresponding author. Cixi Institute of Biomedical Engineering, International Cooperation Base of Biomedical Materials Technology and Application, Chinese Academy of Sciences (CAS) Key Laboratory of Magnetic Materials and Devices, Zhejiang Engineering Research Center for Biomedical Materials, Ningbo Institute of Materials Technology and Engineering, CAS, Ningbo, 315201, China.

** Corresponding author. Cixi Institute of Biomedical Engineering, International Cooperation Base of Biomedical Materials Technology and Application, Chinese Academy of Sciences (CAS) Key Laboratory of Magnetic Materials and Devices, Zhejiang Engineering Research Center for Biomedical Materials, Ningbo Institute of Materials Technology and Engineering, CAS, Ningbo, 315201, China.

E-mail addresses: yangf@nimte.ac.cn (F. Yang), aiguo@nimte.ac.cn (A. Wu).

¹ These authors contributed equally: Hui Du, Fang Yang.

<https://doi.org/10.1016/j.biomaterials.2022.121868>

Received 16 August 2022; Received in revised form 14 October 2022; Accepted 19 October 2022

Available online 29 October 2022

0142-9612/© 2022 Elsevier Ltd. All rights reserved.

1. Introduction

Triple-negative breast cancer (TNBC) represents a huge threat to the human health, and a heavy burden to healthcare systems worldwide, owing to its highly efficient capabilities for migration, invasion and metastasis. The five-year survival rate for patients diagnosed with localized TNBC, not spread beyond the breast, is 91%, but this percentage severely drops to 65% for patients diagnosed at a stage when the TNBC has spread into nearby lymph nodes, and down to 11% for patients in which the TNBC has spread to critical parts of the body, such as bones, lungs or liver [1,2]. TNBC cells are negative for the estrogen receptor (ER), progesterone receptor (PR) and human epidermal growth factor receptor 2 (HER2), thus aren't fueled by hormones that can be specifically targeted, as in other types of breast cancer. Nevertheless, the primary types of anti-cancer treatments, such as surgery, chemotherapy and radiation remain the usual therapeutic options. However, besides their typical side effects and hazards, due to the high chance of relapse and TNBC's partial response to the above-mentioned approaches, alternative therapeutic routes are urgently required. In this context, a wide range of non-invasive and spatiotemporally controlled therapies based on various physical stimuli, such as magnetic fields and light [3], have been developed over the past years as solutions to more effectively fight TNBC. Compared with traditional therapeutic strategies, the pN-level magneto-mechanical force (MMF) generated by magnetic nanomaterials under the effect of an external low-frequency rotating magnetic field (RMF) can be regarded as a powerful tool for the local therapy of deep-seated tumours. The efficiency of such therapies is augmented by other important advantages that derive from RMF actuation, such as safety, non-invasiveness, facile spatiotemporal manipulation and deep tissue penetration [4–6]. Magnetic nanoparticles (MNPs) exposed to low-frequency RMF (0–100 Hz) can perform a series of intricate motions [7], including vibration and rotation, which generate mechanical forces with sufficient strength and amplitude to activate mechanotransduction pathways [8–10], such as changing the cytoskeleton morphology [11], regulating cell adhesion [12], and even inducing cell apoptosis or death [13–15]. In our previous work, we found that the response of magnetic ferrite nanoparticles to external magnetic fields can be significantly improved by the controlled doping of zinc ions [16]. Subsequently, we showed that such MNPs can be used to enable a dual mode of action, where the magneto-mechanical force therapy and chemotherapy can be jointly exploited to overcome the drug resistance of cancer cells [17].

Considering the severe toxic effects of chemotherapeutic approach on normal body tissues, and their limited specificity for cancer cells [18], photothermal therapy (PTT) has emerged as a valuable alternative. In such approaches, photothermal agents are stimulated by light, usually in the near-infrared (NIR) light spectrum to produce local heat in tumour tissues and eradicate pathological cells. Given their capabilities for deep tissue penetration and selective destruction of tumour cells, PTT is considered an efficient and minimally invasive option [19,20]. Most PTT studies to date have focused on the use of light in the NIR-I region (750–1000 nm), while the NIR-II light (1000–1700 nm) window is emerging as a more desirable light source for PTT due to lower photon scattering in tissues, accounting for deeper penetration and further reduced phototoxicity for healthy tissues [21]. Additionally, in order to avoid harsh thermal treatment unfavourably activating the undesirable cell death process known as necrosis, which may trigger inflammatory reactions and cancer metastasis [22], mild NIR-II hypothermia (41–48 °C) allows cancer cells to be preferentially eliminated by apoptosis without damaging normal tissues, a feature that is highly important for clinical application [23,24]. Notably, the temperature modulation of hypothermia is intimately correlated with the expression of heat shock proteins (HSP) [25].

In this work, we demonstrate in both *in vitro* and *in vivo* settings that the combined use of these two complementary and synergistic therapeutic strategies, namely MMF and NIR-II hypothermia, represents an

exquisite route for fighting TNBC. To this end, we have designed and developed a multifunctional magnetic-photothermal converter (MPC) consisting of zinc-doped ferrite nanoparticles ($\text{Zn}_{0.2}\text{Fe}_{2.8}\text{O}_4$ NPs) and polyethylene glycol (PEG). We demonstrate that the MMF generated by the highly efficient magnetic field-mediated MPCs can dramatically inhibit the migration and invasion of MDA-MB-231 cells, and that this therapeutic route can be applied in tandem with NIR-II hypothermia, to result thus in a “double-punch” strategy. Furthermore, we show that these two therapeutic routes are synergistic, with MMF augmenting the outputs of NIR-II hypothermia. To shed light on this, we comprehensively investigate the mechanisms of the MPCs-mediated magneto-photothermal synergistic therapy (MPST) to clarify the intrinsic link between the two treatment modalities (Scheme 1). Given the excellent results of this “double punch” therapeutic scheme and the considerable biocompatibility and biosafety profiles of the MPCs, we consider that the proposed framework holds important potential to pave the way for some future cutting-edge clinical approaches that can successfully fight TNBC as well as cancers in general.

2. Results and discussion

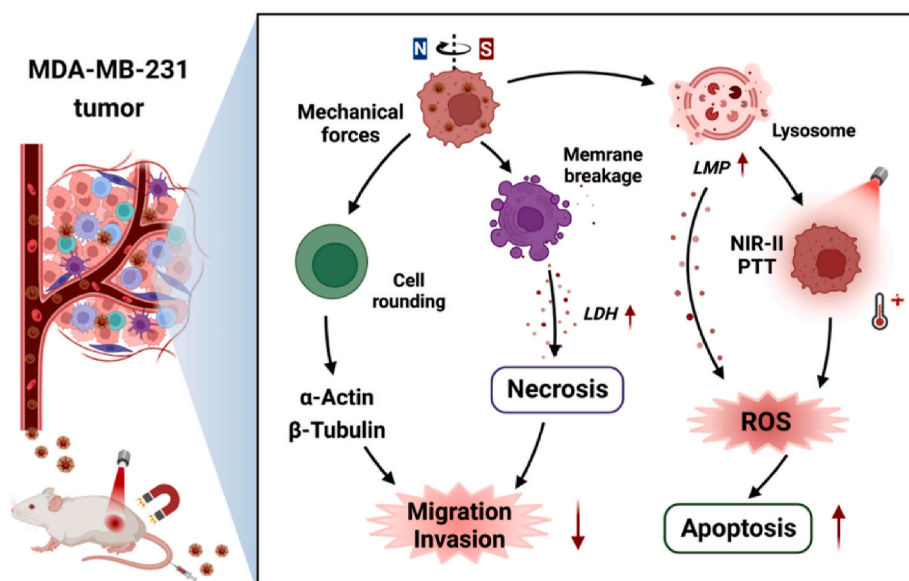
2.1. Design and characterization of the MPCs

The physicochemical properties of the MNPs determine their magnetic responsiveness and NIR photothermal effect. To determine these, a rich palette of investigations has been performed. Approx. 20 nm hydrophilic zinc-doped ferrite nanoparticles were obtained by the high-temperature hydrothermal method [26] and modified with PEG to enhance their dispersibility and biocompatibility (Fig. 1a). Transmission electron microscopy (TEM) revealed that the synthesized MPCs exhibit comparatively good dispersion, with an average size of 80 nm (Fig. 1b and Fig. S1). It should be noted that larger magnetic particles have the potential to generate a more powerful magnetic force, and consequently yield more efficient magneto-mechanical therapeutic effects compared to smaller ones. High-resolution transmission electron microscopy (HR-TEM) and fourier transform infrared spectroscopy (FTIR) demonstrated the successful modification of PEG molecules on the surface of the MPCs (Fig. 1c, g). The selected area electron diffraction (SAED) mode image showed different diffraction rings, indicating a highly crystalline structure (Fig. 1d). As shown in Fig. 1e and Table S1, according to elemental mapping analysis (EDS) and inductively coupled plasma optical spectroscopy (ICP-OES), the ferrites in the MPCs are $\text{Zn}_{0.2}\text{Fe}_{2.8}\text{O}_4$ NPs. The X-ray diffraction (XRD) patterns in Fig. 1f confirmed the spinel cubic structure of the MPCs (JCPDS card no. 22–1012). In addition, the saturation magnetization (M_s) results showed that the MPCs exhibit ferromagnetic behaviour with a coercivity of 32 Oe, while the Zn doping yields an optimal M_s , reaching 86.7 emu/g (Fig. 1h) at room temperature, indicating that MPCs can display superb responsiveness to an applied rotating magnetic field.

An additional set of investigations showed that the MPCs exhibit significant absorption in the NIR-II window (Fig. 1i). Under 1064 nm laser light irradiation (1.5 W/cm^2) for 10 min, the aqueous solution of MPCs showed a dramatic increase in temperature of 20 °C (Fig. S2a). Further assays indicated that the temperature rise profiles and infrared images of MPCs were positively correlated with the concentration of MPCs and laser power density, revealing their controllable photothermal behaviour (Fig. 1j and Fig. S2b). Remarkably, the MPCs exhibited excellent thermal stability after five heating and cooling cycles under laser irradiation (Fig. 1k). According to the change in temperature, the photothermal conversion efficiency (PCE) in the NIR-II region was calculated at 11.65% (Fig. S2c).

2.2. MPCs-mediated MMF effects on cell fate

To objectively assess the extent of cancer cell damage achieved by MPCs-mediated MMF effects under an RMF, the intrinsic cytotoxicity of



Scheme 1. Schematic illustration of the MPCs-mediated magneto-photothermal synergistic strategy (MPST) for TNBC therapy. The zinc-doped ferrite nanoparticles were modified to obtain biocompatible nanocomposites (MPCs) with excellent magnetism and NIR-II photothermal abilities. After being internalized into TNBC cells, MPST treatment was carried out. Under a 15 Hz rotating magnetic field, the generation of MMF was found to effectively inhibit the migration and invasion of MDA-MB-231 cells, while also enhancing the lysosomal membrane permeability and elevating the intracellular reactive oxygen species (ROS), making cells sensitive to the subsequent heating. The second therapeutic route based on exposure to NIR-II hypothermia was found to elevate intracellular oxidative stress, accelerating cell death. The synergistic effect between MMF and NIR-II PTT was demonstrated as being highly effective both *in vitro* and *in vivo*.

MPCs was first investigated. The viability of MDA-MB-231 cells remained above 80% when incubated with MPCs (800 $\mu\text{g}/\text{mL}$) for 24 h, indicating that the MPCs possess excellent biocompatibility (Fig. 2a). As shown in Fig. 2e, MPCs (300 $\mu\text{g}/\text{mL}$) were completely internalized by MDA-MB-231 cells after 12 h of co-incubation. TEM imaging showed that the MPCs mainly tend to localize in lysosomes and partially in the cytoplasm (Fig. 2f). Under the demonstrated premise of biocompatibility and internalization, the MMF effects of the MPCs were further investigated *in vitro*.

As shown in Fig. 2b, c, the strength and the action time of the magnetic field were found to play important roles in destroying cancer cells under the same treatment conditions, indicating that the stronger the magnetic field or the longer the action time of the RMF, the lower the cell viability. Conversely, exposure of pure cells (without internalized MPCs) to RMF did not inhibit their viability (Fig. 2b and c). Interestingly, under the effect of RMF at 60 mT for 2 h, the cell viability showed a trend of decreasing at first and afterwards increasing with the increased magnetic field frequency, Fig. 2d, indicating that MPCs and RMF reached the maximum synchronization frequency at 15 Hz [27]. Hence, MPCs-mediated MMF under this setting resulted in the highest killing rate, namely a cell lethality ratio of 23%.

Furthermore, scanning electron microscopy (SEM) imaging was used to reveal how the extent of cell membrane damage resulting from MMF therapy correlates with the RMF action time (Fig. 2g). The perforation of the cell surface by the MPCs becomes more obvious with increased RMF exposure time, as evidenced by the significantly increased number and diameter of the cellular membrane holes. Complete cleavage of the cell membrane can be observed for part of the cells treated with RMF for 2 h. Additionally, damage to the cell membrane was also found to cause the release of important intracellular components such as lactate dehydrogenase (LDH). In this respect, Fig. 2h shows that the release of intracellular LDH increases dramatically over the duration of RMF. Considering that the perforation of the cell membrane and the consequent discharge of more intracellular components eventually leads to cell death, the therapeutic effects of MPCs-mediated MMFs in terms of cancer cell killing are obvious.

2.3. MPCs-mediated MMF effects on cell migration and invasion

In comparison to assessing the potential of MPCs to kill cancer cells by MMF effects, objective quantification of their capacity to suppress the migration and invasion of tumour cells (Fig. 3) was significantly more

challenging, given the high metastatic potential of the MDA-MB-231 cells (the considered TNBC cell line). Such cells are vigorously aggressive, resistant to chemotherapeutic agents such as dasatinib [28], and exhibit unanchored growth independent of growth factors [29]. The cytoskeleton provides stability for cell morphology and participates in critical processes such as cell mitosis, endocytosis and motility, performing an essential role in the migration and invasion of tumour cells, for which actin filaments and microtubules are the main components [30]. Based on this, as shown in Fig. 3a, b, β -tubulin and F-actin were stained by immunofluorescence and ghost pen loop peptide, respectively. Using confocal laser scanning microscopy (CLSM), untreated MDA-MB-231 cells, with their characteristic shuttle-shaped growth pattern, were found to be structured by organized β -tubulin and F-actin architectures with some filopodia or lamellipodia formation (Fig. 3a, b). As the RMF (60 mT, 15 Hz) exposure time was prolonged, the cells treated with MPCs crumpled into round shapes, which was accompanied by remarkable changes in the cytoskeleton, resulting in more skeletal proteins being focused on the outer edges of the cells and the disappearance of the cell membrane folds, together with the filamentous and lamellar pseudopods.

The significant changes observed in the cytoskeleton structure, motivated us to further evaluate the effect of MMF on the migration and invasion of MDA-MB-231 cells (Fig. 3c), which we accomplished by cell wound healing and transwell invasion assays. The migration ability of cancer cells was assessed by the average decrease in the distance between wound edges at different time points (0 h, 12 h, 24 h, 36 h) in the presence or absence of MMF stimulation. The cell wound healing assay results displayed in Fig. 3c, d and Table S2 revealed that cells treated with MMF significantly repressed wound healing with a 67.63% decrease in cell migration compared to the pure cell group at 36 h. Consistent with this finding, we also identified by transwell invasion assays (Fig. 3c, e and Table S3) that the invasive capacity of the cells dramatically decreased to 71.82% of the original level within 36 h after MMF treatment. Our investigations showed that treatment of MDA-MB-231 cells with MPCs has no influence on cell migration and invasion in the absence of RMF.

2.4. MPCs-mediated MPST effects on cell fate *in vitro*

In previous sections, we showed that the MPCs-mediated MMF effects under RMF exposure inhibit the growth, migration and invasion of tumour cells, to some extent. Here we demonstrate a strategy for using

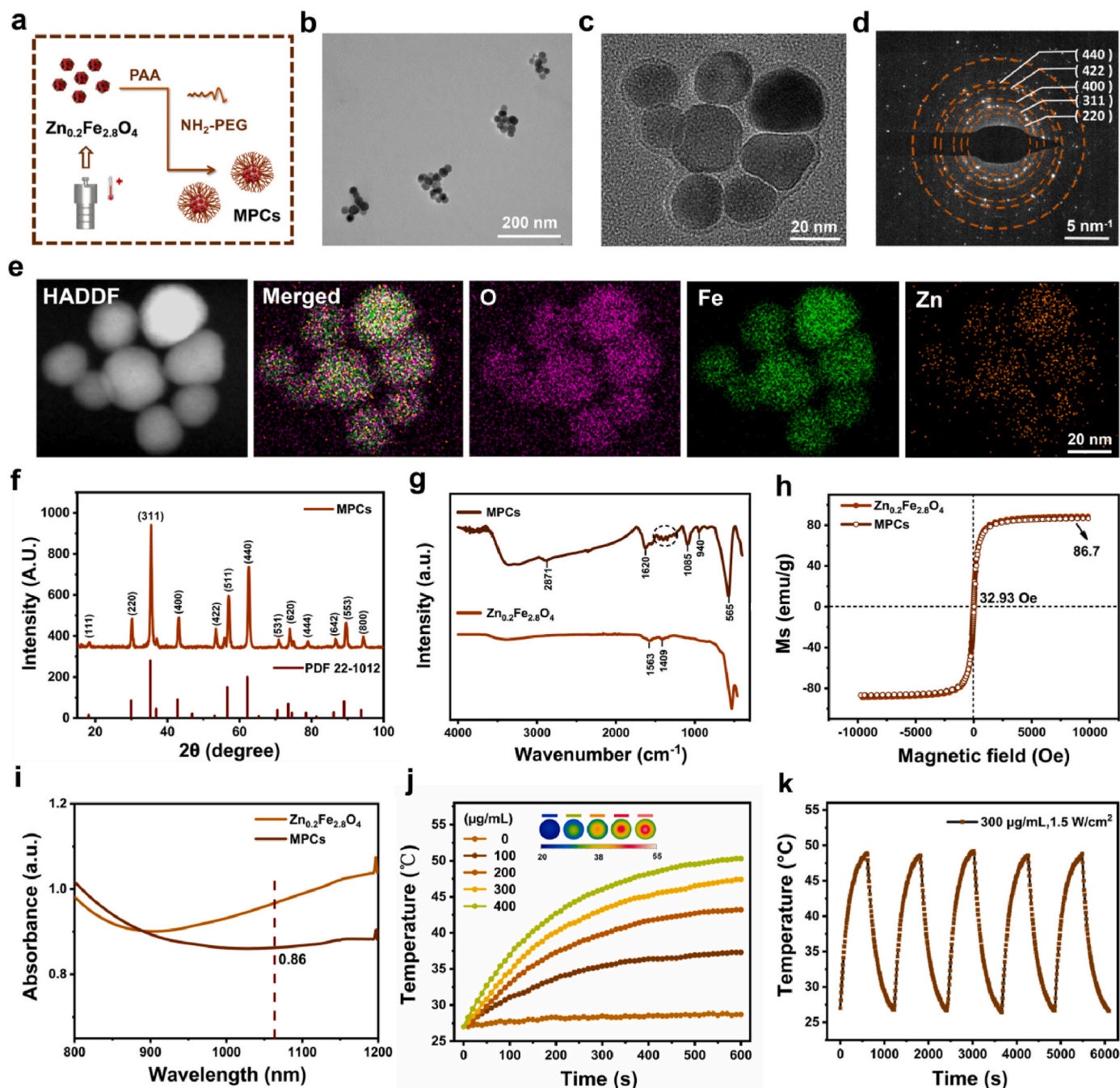


Fig. 1. Synthesis and characterization of the MPCs. (a) Schematic illustration of the preparation process. (b) TEM image of the MPCs. (c) HR-TEM image of MPCs showing that the surface of MNPs is wrapped with a PEG layer of uniform thickness. (d) The SAED mode. (e) EDS analysis showing that the Zn, Fe and O species were uniformly distributed on the individual MPC nanoparticles. (f) XRD spectrum at room temperature. (g) FTIR spectra demonstrating the successful modification of PEG on the surface of $\text{Zn}_{0.2}\text{Fe}_{2.8}\text{O}_4$ NPs, where 940 cm^{-1} and 1085 cm^{-1} both represent the bending vibration peaks of the C–H bond, 1620 cm^{-1} and 2871 cm^{-1} are indicated as the stretching vibration peaks of C=O and C–H bonds, respectively, and the dashed circle indicates the C–C skeleton vibration peaks. (h) Ms results and (i) NIR absorption spectra of MPCs ($300\text{ }\mu\text{g/mL}$) and $\text{Zn}_{0.2}\text{Fe}_{2.8}\text{O}_4$ NPs ($300\text{ }\mu\text{g/mL}$) at 300 K , respectively. (j) Photothermal conversion of MPCs at 1064 nm (1.5 W/cm^2) at different concentrations ($0, 100, 200, 300, 400\text{ }\mu\text{g/mL}$). (k) Temperature variation over 5 on/off cycles of laser excitation.

MMF in concert with NIR-II hypothermal ablation, a second, complementary therapeutic route that augments the outputs of the first therapeutic layer, resulting in a highly efficient “double-punch” weapon against TNBC, the MPST. To this end, we exploit the excellent NIR-II photothermal properties of the MPCs, and use low-temperature PTT in the NIR-II window (1064 nm) to eliminate surviving MDA-MB-231 cells that were previously treated by MMF. We observe that PTT effects are facilitated by prior MMF ones, which makes the two therapies highly synergistic.

Under 1064 nm laser irradiation (1.5 W/cm^2), the viability of cells treated with MPCs was observed to decrease substantially with increased exposure time (Fig. 4a), while pure cells were virtually unaffected by the NIR light irradiation, corresponding to the infrared images shown in Fig. 4b. To further evaluate the effectiveness of the MPST strategy, MPST was conducted at different PTT times ($0, 4, 8, 12$ and 16 min) with an optimized MMF (15 Hz , 60 mT , 2 h). The calculated Q values are observed to exhibit an increase then decrease trend, reaching a maximum of 1.39 at an irradiation time of 8 min , which is higher than

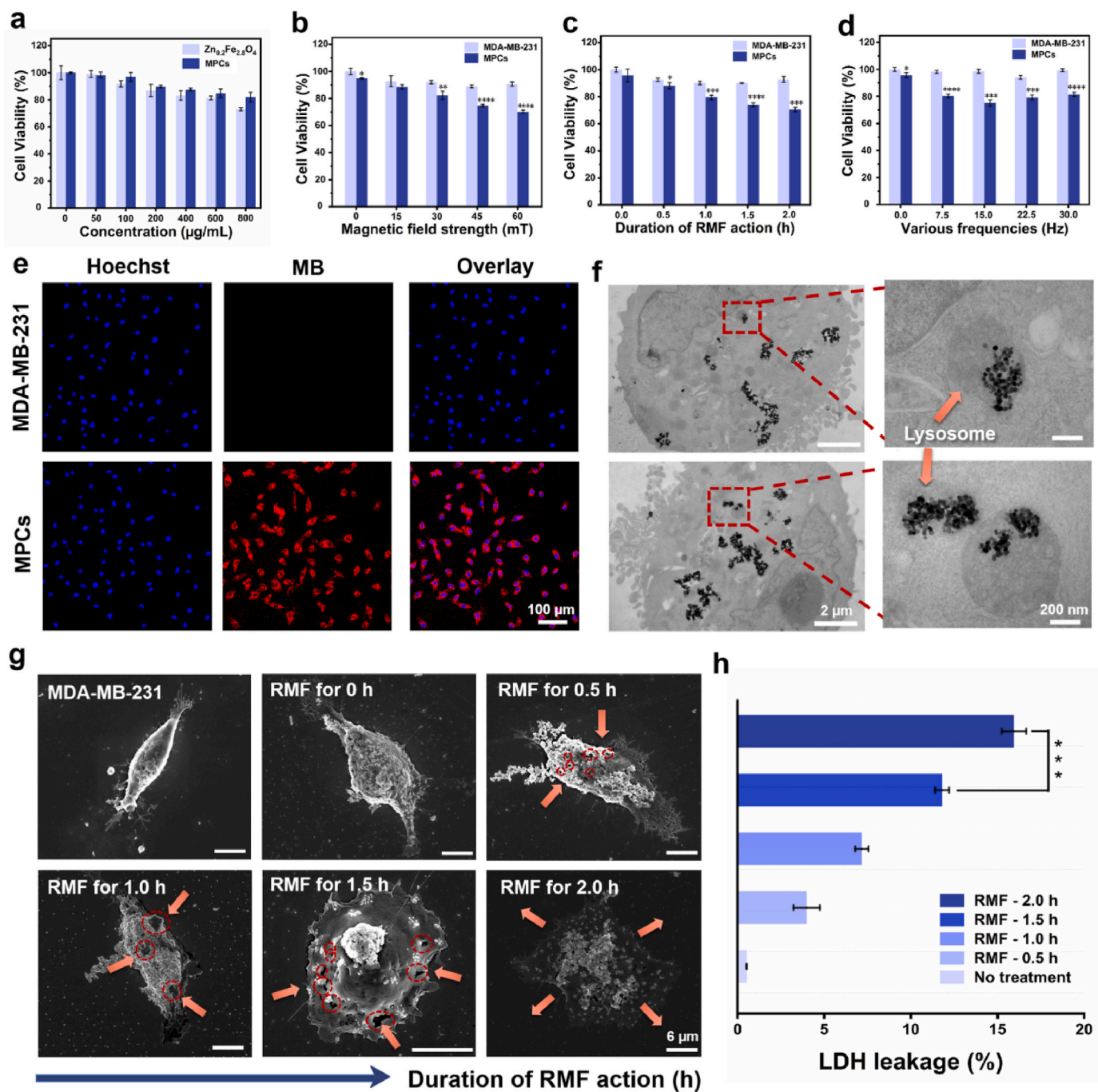


Fig. 2. MDA-MB-231 cancer cell death induced by MPCs by magneto-mechanical force effect. (a) Cell viability of the MDA-MB-231 after co-incubation with different concentrations of MPCs for 24 h. The viability of cells treated with MPCs-mediated (300 $\mu\text{g/mL}$) MMF at different strengths (b), durations (c) and frequencies (d) of RMF, respectively. * $P < 0.1$, ** $P < 0.01$, *** $P < 0.001$, **** $P < 0.0001$ indicates a statistical difference between the MDA-MB-231 and MPCs groups under the same conditions. (e) The uptake of MPCs (300 $\mu\text{g/mL}$) by MDA-MB-231 cells following 12 h of co-incubation (Scale bar: 100 μm). (f) TEM images showing the localization of MPCs within MDA-MB-231 cells (Scale bar: 2 μm ; Zoom in: 200 nm). (g) SEM images of cells under various RMF exposure intervals (Scale bar: 6 μm). (h) The release of LDH from cells after treatment with MPCs (300 $\mu\text{g/mL}$) upon exposure to RMF with different action time. *** $P < 0.001$ indicates a statistical difference between the two groups. Data are expressed as mean \pm standard deviation. Error bars are based on the results of at least three independent experiments per group.

the determined threshold for the synergistic effect index of 1.15 [14] (Fig. 4c and Table S4). Therefore, the treatment time in the subsequent *in-vitro* experiments was set to the optimized value of 8 min for PTT, accompanied by a temperature increase to 47.3 $^{\circ}\text{C}$, at which the enhancement of intracellular heat resistance due to HSP overexpression could be effectively avoided (Fig. 4b) [31,32]. The CCK-8 assay results displayed in Fig. 4d showed that over 80% of cancer cells were killed after MPST treatment, which yielded a considerably higher killing rate

than those observed for independent MMF (23%) and PTT (40%). These results reflect the valuable potential of the synergies occurring between MMF and PTT therapies.

To further investigate the mechanism by which the “double-punch” MPST therapeutic strategy achieves cancer cell death, CLSM imaging was employed to evaluate the overall level of reactive oxygen species (ROS) of *in vitro* MDA-MB-231 cells stained with a 2,7-dichlorodihydrofluorescein diacetate (DCFH-DA) probe (Fig. 4e). Besides the

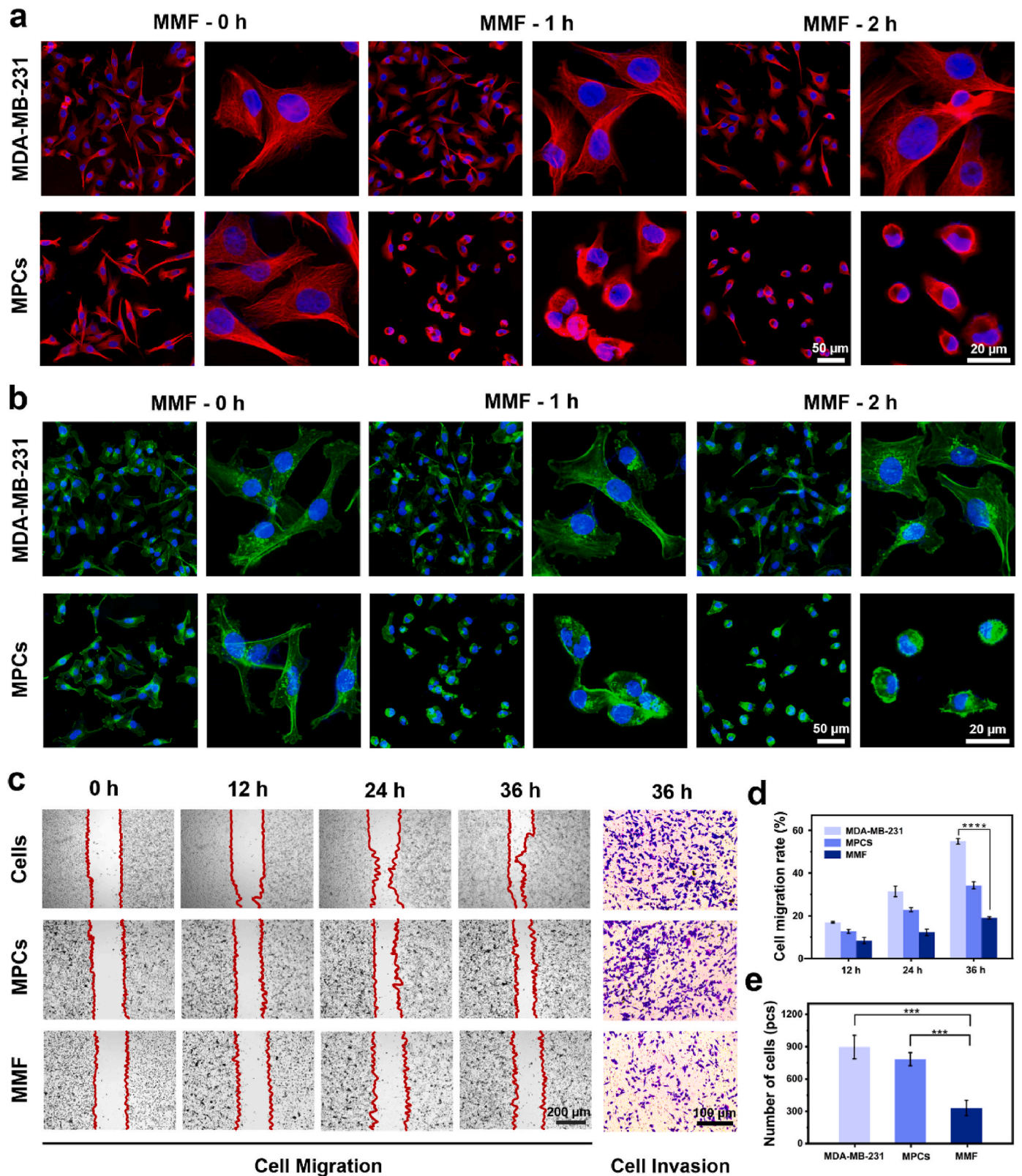


Fig. 3. MPCs-mediated MMF effects under RMF exposure modify the cells' cytoskeleton in a manner that inhibits their migration and invasion. Representative CLSM images of (a) microtubule network and (b) actin cytoskeleton in control and MPCs-treated MBA-MD-231 cells at various RMF exposure time. β -tubulin (red), F-actin (green) and DAPI-stained nuclei (blue). Scale bar: 50 μ m; Zoom in: 20 μ m. (c) The cell wound healing assays at different time points (0 h, 12 h, 24 h and 36 h) and transwell invasion assays at 36 h of MDA-MB-231 cells treated with MPCs-mediated MMF effects under RMF (the black scale bar: 200 μ m and 100 μ m, respectively). (d) Cell wound healing assay: evaluation of migration distance within 36 h (n = 3). (e) Transwell invasion assay: number of cells crossing the chambers over 36 h (n = 3). *** P < 0.001, **** P < 0.0001 indicates a statistical difference between the two groups. Data are expressed as mean \pm standard deviation. Images are representative of three independent experiments. (For interpretation of the references to colour in this figure legend, the reader is referred to the Web version of this article.)

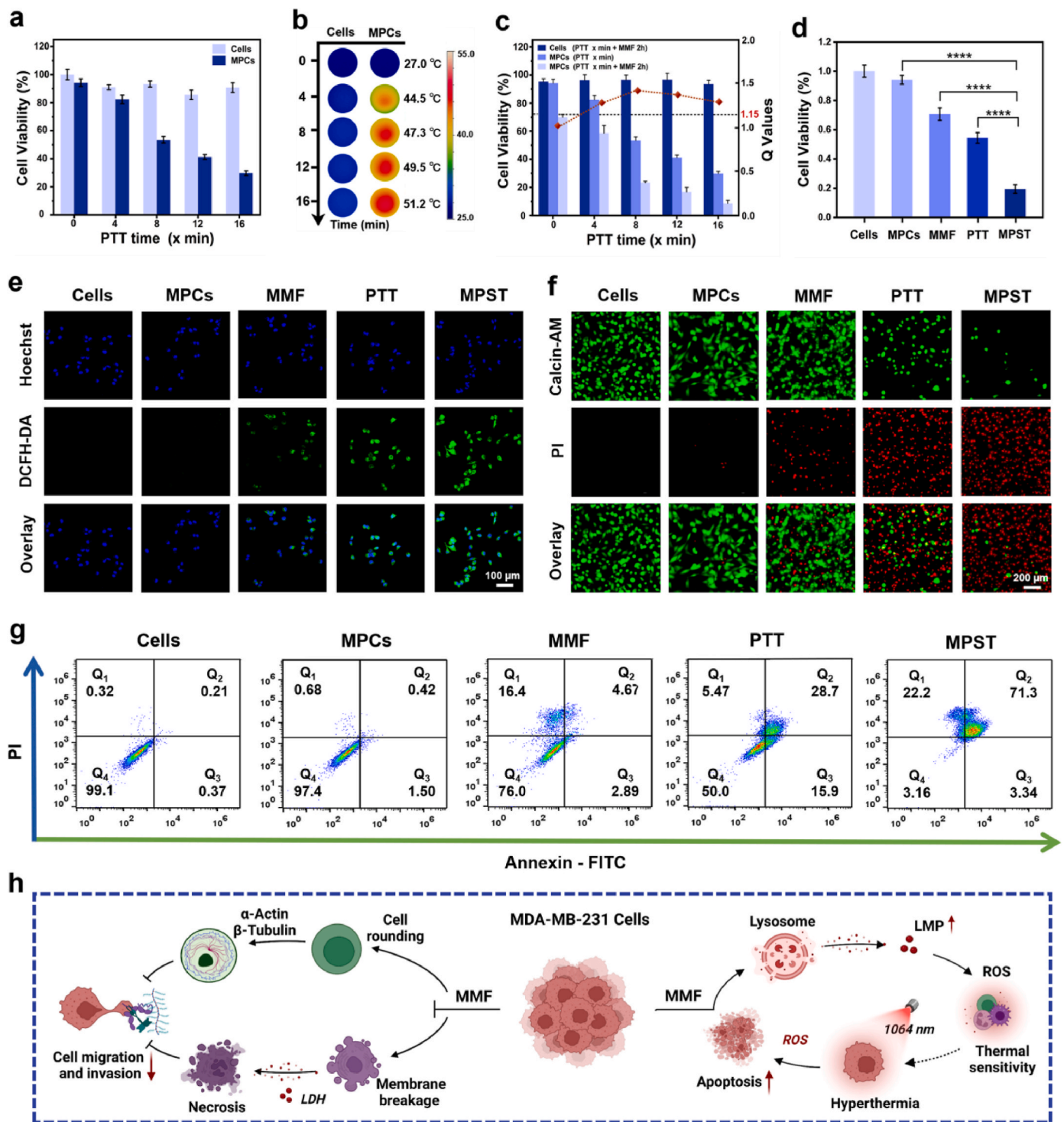


Fig. 4. MPST effect: MPCs induce MDA-MB-231 cell death by in-tandem, synergistic, use of MMF and NIR-II hypothermia. *In vitro* viability (a) and infrared images (b) of cancer cells treated with MPCs-mediated enabled (300 $\mu\text{g}/\text{mL}$) NIR-II hypothermia at different irradiation times (0, 4, 8, 12, 16 min) with a 1064 nm laser. (c) The viability of cancer cells and Q values under MPST treatment consisting of 2 h MMF and varied PTT time. $Q \geq 1.15$ demonstrate the existence of a synergistic effect between the two therapeutic routes. (d) Therapeutic effects on MDA-MB-231 cells of MPCs-mediated MMF, PTT and MPST therapies assessed by the Cell Counting Kit assay. Relevant treatment parameters are RMF with 15 Hz, 60 mT, 2 h and PTT with 1.5 W/cm^2 , 8 min. Statistical analysis was obtained using a *t*-test, $****p < 0.0001$ ($n \geq 3$). (e) CLSM images of ROS levels in MDA-MB-231 cells treated with MPCs upon different therapeutic modalities (Scale bar: 100 μm). (f) The Calcein AM/PI-costained of cells after various treatments (Scale bar: 200 μm). (g) The AnnexinV-FITC/PI analysis of cell death patterns under exposure to diverse treatments using flow cytometry. (h) Mechanistic diagram of the MPST therapy *in vitro*.

significantly elevated ROS levels of the PTT and MPST-treated cells, we also noticed an unexpected increase in the intracellular ROS levels after MMF treatment. This suggests that the mechanical stimulation of cells can effectively up-regulate their biochemical ROS signalling. We hypothesized that this may be correlated with an enhanced permeability of the lysosomes [33,34]. To validate our hypothesis, we assessed the changes in the subcellular structure and lysosomal permeability (LMP) using acridine orange (AO) fluorescence detection reagents. Generally, in intact lysosomes, AO exists as a protonated oligomer with red fluorescence: the manifested red fluorescence spots gradually diminish with the increase of LMP (Supplementary, Fig. S3). In comparison with the pure cell group (without internalized MPCs), and with the MPCs group

without exposure to RMF or NIR light, a significant weakening of the red fluorescent spots was observed in the MMF and PTT groups, implying that individual MMF or PTT treatments were able to disrupt the lysosomal membrane by mechanical force or heat, respectively. Furthermore, for the MPST group, the red fluorescent spots were no longer visible, indicating a greater extent of LMP.

The aggravated oxidative damage to tumour cells in the mid-to-late stage of apoptosis and death under various treatments was further verified by Calcein Acetoxymethyl Ester (AM)/propidium iodide (PI) costaining (Fig. 4f). To further explore the mechanism of cancer cell death after treatments with MMF, PTT and MPST, we used Annexin V-fluorescein isothiocyanate (FITC)/PI costaining by flow cytometry

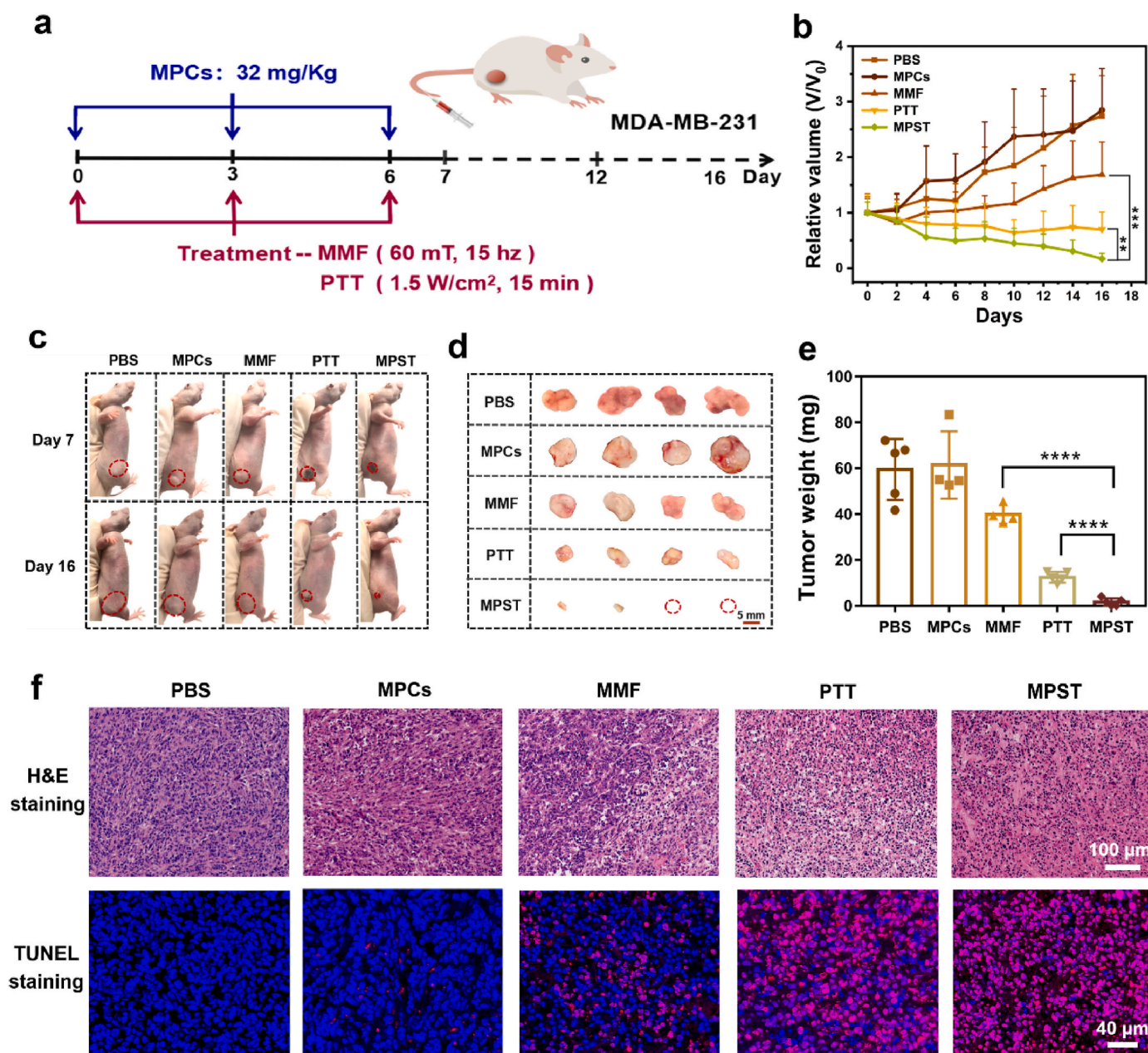


Fig. 5. The therapeutic effectiveness of MPST in MDA-MB-231-bearing mice. (a) Schematic diagram of the treatment procedure *in vivo*. MPCs were injected intravenously and treated on days 0, 3 and 6 for three times, with the parameters of 60 mT, 15 Hz, and 2 h for MMF and 1.5 W/cm², 8 min for PTT. (b) The relative tumour volume of mice in various treated groups (n ≥ 5). (c) Pictures of mice with tumours on day 7 and day 16. Pictures (d) and weights (e) of tumours from each treatment group were obtained after dissection (Scale bar: 5 mm). Statistical analysis was obtained using a *t*-test, ***P* < 0.01, ****P* < 0.001, *****P* < 0.0001 (n ≥ 4). (f) H&E staining and TUNEL staining of pathological changes in tumour tissues from various treatments, where TUNEL staining can detect apoptosis of cells. FITC-dUTP stained cells in apoptosis (red) and DAPI-stained nuclei (blue). Scale bar: 100 μm and 40 μm. (For interpretation of the references to colour in this figure legend, the reader is referred to the Web version of this article.)

(Fig. 4g), where AnnexinV can conjugate to phosphatidylcholine (PS) and translocate from the interior to the exterior of the plasma membrane during early apoptosis, while PI is utilized to assess the integrity of the cell membrane, signalling late apoptotic or necrotic cell death [35,36]. According to these analyses, the cell death mode of the MMF group was primarily mechanical necrosis, while for the PTT and MPST groups, late-stage apoptosis was predominant.

From the available results, it can be concluded that in the presence of RMF, the MMFs generated by the massive accumulation of intracellular MPCs cause direct mechanical destruction to the cell membrane, leading to partial cell mechanical necrosis, which further inhibits cell migration and invasion. The MMF effects were also shown to disrupt lysosomes, causing a massive release of internal proteolytic enzymes and acids, which lowers the cytoplasmic pH and induces oxidative stress reactions in cells, thereby making them more sensitive to external stimuli (e.g., heat). Thus, the therapeutic potential of subsequent hypothermia in the NIR-II region was considerably augmented, accompanied by high levels of ROS generation, hence accelerating the apoptosis of cancer cells (Fig. 4h).

2.5. Therapeutic efficiency of MPST *in vivo*

Following the exploration of the MPST mechanisms occurring at the cellular level *in vitro*, an MDA-MB-231 subcutaneous tumour model was constructed and applied to evaluate the therapeutic effects of MPST *in vivo*. When the tumour volume reached 100 mm³, the MPCs were administered intravenously to mice three times on days 0, 3 and 6 with a dose of 30 mg/kg per injection, satisfying the biosafety profile (Fig. 5a, Fig. S4, 5). The accumulation of MPCs at the tumour site was indirectly determined by monitoring its heating upon 1064 nm laser irradiation every 2 h. After 8 h of MPCs injection, the temperature rose significantly, and following this interval, no additional increase could be observed, which demonstrated that the accumulation of MPCs at the tumour site reached the maximum level at this time point (Fig. S6). Accordingly, after 8 h of intravenous injection, the MPCs-mediated treatments were performed three times every two days, from day 0 to day 6 with treatment parameters of 60 mT, 15 Hz, and 2 h for MMF and 1.5 W/cm², 15 min for PTT, respectively. Noteworthy, the RMF parameters and NIR-II laser power in this study were both positioned in the safe range [37,38].

The body weight and tumour size of MDA-MB-231-bearing mice were monitored daily for 16 days. The body weight of the mice was maintained essentially steady (Fig. S7, supporting information). MMF had an inhibitory effect, while the effect of PTT was enhanced and significantly reduced tumour size. Importantly, tumours in the MPST group were entirely eliminated (Fig. 5b–d). Moreover, the quantitative analysis of tumour weight was consistent with the tumour images (Fig. 5e). Additionally, Hematoxylin-Eosin (H&E) and TdT-mediated dUTP nick end labelling (TUNEL) staining revealed that the tumour tissue was found to be entirely necrotic under MPST treatment. MMF alone did not prevent cancer cells from developing into tumours whereas low-temperature PTT remarkably reduced tumour size, which was accompanied by massive tumour tissue necrosis (Fig. 5f).

To investigate the metabolism of MPCs after 16 days in mice, Prussian blue dye was applied to stain the MPCs. Fluorescent signals corresponding to this contrast agent were not observed at the tumour site, while signals originating from the liver and spleen indicated some extent of MPC accumulation in these organs (Fig. S8). However, the overall results obtained by H&E staining, blood routine and blood biochemical analysis, displayed in Figs. S9 and S10, no apparent MPCs-induced damage was discovered in the heart, liver, spleen, lung, and kidney tissues, indicating a good safety profile for this MPST enabling therapeutic agent. The *in vivo* results reveal that the MPCs-mediated MPST strategy has a significantly destructive effect on TNBC tumours and that this treatment approach is likely to have minimal hazard concerning the patient's safety, according to biosafety assays performed in mice. Collectively, these findings propose MPCs-mediated MPST as a

potential candidate for a future cutting-edge clinical therapy for fighting TNBCs, and cancers in general.

3. Conclusion

In summary, to efficiently treat TNBC, we designed and demonstrated a custom-tailored strategy exploiting the synergisms occurring between the therapeutic effects of magneto-mechanical forces and photo-thermal damage induced by MPCs that feature superb capacities to accurately respond to external physical stimuli. We have first developed a versatile MPC with excellent biocompatibility as a force-thermal converter, capable of transforming external magnetic and light in the NIR-II window into force and heat, respectively, in a well-controlled manner. Second, we demonstrated that the MMF generated by MPCs under the effect of RMF significantly diminishes the migration and invasion capacities of tumour cells by 67.63% and 71.82%, respectively, via changing the cytoskeleton morphology while exerting a significant inhibitory effect on the growth of MDA-MB-231 cells. Furthermore, we also found that the MMF generated by the massive accumulation of intracellular MPCs caused direct mechanical destruction to their cell membrane, leading to partial cell mechanical necrosis, and disruption of intracellular lysosomes. This latter outcome resulted in increased LMP levels and the related release of large amounts of protein hydrolases, which further induced intracellular oxidative stress. These results were found to be synergistic with the NIR-II hypothermal effects, enhancing their extent and significantly augmenting the outputs of the PTT strategy. Applying the PTT treatment after MMF led to significantly more elevated levels of intracellular ROS compared to the case where MMF was not previously applied, and also massively accelerate the induction of apoptosis. Therefore, the demonstrated MPST strategy leads to a chain reaction of the cell membrane, skeletal proteins, subcellular organelles, and biological signals, which results in remarkable therapeutic success against TNBC in both *in vitro* and *in vivo* settings. Although tested on TNBC, the proposed framework has high potential to be generalized to successfully fight against other cancer variants, in a less invasive and hazardous way than current state-of-the-art methods.

4. Materials and methods

4.1. Materials and reagents

Ferrous sulfate heptahydrate (FeSO₄·7H₂O), sodium citrate, 1-(3-Dimethylaminopropyl)-3-ethylcarbodiimide hydrochloride (EDC) and *N*-hydroxy succinimide (NHS) were purchased from Aladdin Industrial Corporation (Shanghai, China). The zinc acetate dihydrate (Zn (Ac)₂·2H₂O) was obtained from Energy Chemical (Shanghai, China). Monohydrazine (N₂H₄·H₂O) was purchased from Sinopharm Chemical Reagent Co., Ltd. (Shanghai, China). Polyacrylic acid (PAA, MW: 2000 Da) and Methylene blue (MB) were obtained from Macklin (Shanghai, China). Amino-modified polyethylene glycol (mPEG-NH₂, MW: 2000 Da) was purchased from Yare Biotech, Inc. (Shanghai, China). Cell Counting Kit-8 (CCK-8) was purchased from Apex BIO (America). Hoechst 33342 was obtained from Biosharp (Anhui, China). Reactive Oxygen Species Assay Kit (SOO33S), Calcein/PI Cell Viability/Cytotoxicity Assay Kit (C2015S), Lactate dehydrogenase cytotoxicity (LDH) assay kit (C0017) and Annexin V-FITC Apoptosis Detection Kit (C1067S) were obtained from Beyotime (Shanghai, China). The lysosomal membrane permeability (LMP) assay kit was obtained from Chen Gong Biotechnology Co., Ltd. (Shanghai, China). All other chemicals and solvents are of analytical grade (AR) and can be used directly without further purification.

4.2. Synthesis of the Zn_{0.2}Fe_{2.8}O₄ MNPs

First, 1.8 mmol FeSO₄·7H₂O and 3.64 mmol Zn (Ac)₂·2H₂O were dissolved in 20 mL of deionized water, and 1.94 mmol citric acid was added quickly via magnetic stirring to obtain a uniform solution. At this

point, 2.5 mL of 10 mol L⁻¹ N₂H₄·H₂O was added dropwise to the mixture and mechanically stirred for 30 min. Then, the mixture was transferred to a 50 mL capacity Teflon-lined autoclave and heated at 200 °C for 16 h via using a high-temperature oven and naturally cooled to room temperature. In a further step, the supernatant was removed, and the precipitate was centrifuged at 8000 rpm for 7 min and washed 6 times with alternating distilled water and absolute ethanol. Finally, it was stored by freeze-drying for 12 h and then protected from light.

4.3. Synthesis of the MPCs

Initially, 5 mL of the prepared Zn_{0.2}Fe_{2.8}O₄ MNPs (2 mg/mL) were dispersed into 10 mL of PAA (5 mg/mL) under sonication conditions and mechanically stirred for 2 h. Secondly, the reactants were centrifuged and washed three times with deionized water. After that, 50 mg of mPEG-NH₂ was added to it and sonicated for 30 min. Then, 15 mg each of EDC and NHS were added sequentially and sonicated for 30 min. Finally, after 12 h of mechanical stirring, the reaction products were washed three times with deionized water to obtain MPCs.

4.4. Cellular viability using the MMF assay

The CCK-8 assay was used to assess the effect of treatment via MMF. Briefly, cells were seeded on 96-well plates (1 × 10⁴ cells per well) and incubated for 12 h to adhere to the well. Then, MPCs (300 µg/mL) were added and co-incubated for 12 h and treated using a magnetic rotation platform with different magnetic field strengths (0, 15, 30, 45, 60 mT), different action times (0, 0.5, 1, 1.5, 2 h) and different rotation frequencies (0, 7.5, 15, 22.5, 30 Hz). After this, the cells were put back into the incubator and continued to incubate for 4 h. CCK-8 (10 µL) was added and continued to incubate at 37 °C for 1.5 h. The absorbance at 450 nm was finally measured using an enzyme marker.

4.5. Analysis of cell morphology by SEM

The changes in morphological characteristics of MDA-MB-231 cells before and after magnetic treatment were analyzed by scanning electron microscopy. Briefly, MDA-MB-231 cells (1 × 10⁵ pcs/mL) were seeded on in silico (~1 × 1 cm²) and cocultured with MPCs (300 µg/mL) for 12 h. Secondly, redundant material was washed off and cells were fixed with 2.5% glutaraldehyde at 4 °C for 2 h, followed by 2 washes with PBS (10 min each). Cells were dehydrated with a gradient sequence of ethanol (30%, 50%, 70%, 90% and 100%) (15 min for each concentration). Finally, the prepared dried samples were observed by SEM at 10 kV.

4.6. LDH release assays

The results of LDH release from MDA-MB-231 cells cultured with MPCs were evaluated for 12 h at various times of RMF action. The absorption intensity at 490 nm of the cell culture medium containing the LDH test working solution was measured and the LDH leakage was calculated from LDH leakage (%) = [(absorbance of treated cells - absorbance of control cells)/(absorbance of maximally enzymatically active cells - absorbance of control cells)] × 100. The assay was performed according to the corresponding instructions provided by the kit manufacturer.

4.7. Immunofluorescence staining

To visualize the effect of the magnetic force on the cytoskeleton, immunofluorescence microscopy experiments were conducted on the MDA-MB-231 cell lines. Cells (2 × 10⁵ pcs) were seeded on crawl sheets (2 × 2 cm²) and co-incubated with MPCs (300 µg/mL) for 12 h. Secondly, they were treated with RMF of different action times and immediately fixed with 4% FBS for 30 min. Next, the slices were shaken

dry and circled in the middle of the coverslip with a histochemical pen, and 50–100 µL of the film-breaking solution was added and incubated for 10 min at room temperature, washed 3 times with PBS for 5 min each time. Following this, cells were incubated with the primary antibody, anti-beta-tubulin mouse monoclonal antibody (1:200) at 4 °C overnight. After washing 3 more times with PBS, CY3-labeled secondary antibodies of the corresponding species were added to them and incubated for 50 min at room temperature, protected from light. Then, a TSA signal amplification reagent was added for 3–5 min, followed by 3 washes with PBS and 50–100 µL of FITC-labeled ghost cyclic peptide working solution was added to the cells and incubated for 2 h at room temperature. In addition, the nuclei of the cells were stained using DAPI. Finally, the slide was shaken dry with the cell side down and sealed on a slide with an anti-fluorescence quenching sealer, and placed under a fluorescence microscope (ECLIPSE E100, NIKON) for observation and image acquisition.

4.8. Cell migration assay

Firstly, MDA-MB-231 cells (1.2 × 10⁶ pcs) were seeded on a six-well plate containing a scratch assay insert. Next, the cells were co-incubated with MPCs (300 µg/mL) for 12 h, washed three times with PBS and replaced with serum-free DMEM. Afterwards, the scratch images were taken by a reverse fluorescence microscope (DMIL LED, Leica) at different time points (0, 12, 24 and 36 h) after magnetic treatment. Finally, the scratch area was calculated using Image J. The ability of MMF to inhibit cell migration (AMICM) is calculated by the following formula, where R_{Cell} and R_{MMF} represent the respective migration rates.

$$AMICM = (1 - R_{MMF} / R_{Cell}) \times 100\% \quad (1)$$

4.9. Cell invasion assay

The matrigel was first diluted to 250 µg/mL with serum-free DMEM at 1:40. Secondly, 100 µL of the diluted solution was applied to the upper layer of Transwell chambers and placed on a 24-well plate. After placing it in the incubator for 1 h to make the matrix gel sufficiently solidified, the upper chamber culture was aspirated and 200 µL of serum-free culture medium containing MDA-MB-231 cells (5 × 10⁶ pcs) was added to it. After that, the upper chamber was carefully placed with forceps on top of the lower chamber containing 15% serum and placed back in the incubator for 36 h. After fixing with 4% FBS at room temperature for 30 min, the upper chamber was washed twice with PBS and stained with 0.5% crystal violet for 15 min. The upper chamber was washed with PBS to remove excess crystal violet and wiped clean with a cotton swab. Finally, they were observed by light microscopy and counted by Image J. The ability of MMF to inhibit cell invasion (AMICI) is calculated by the following formula, where N_{Cell} and N_{MMF} represent the number of cell invasions, respectively.

$$AMICI = (1 - N_{MMF} / N_{Cell}) \times 100\% \quad (2)$$

4.10. Effect of MPST

First, 1.2 × 10⁵ MDA-MB-231 cells were seeded in 96-well plates for 12 h. Then MPCs were added and incubated for 6 h. For the PTT group, cells were treated with photothermal treatment for different action times (0, 4, 8, 12 and 16 min) and then placed back in the incubator for 6 h. For the MPST group, cells were treated with MMF for 2 h and then placed back in the incubator for 4 h. Then, the next steps for the MPST group were the same as those for the PTT group. Finally, the cells were then assayed for activity with the CCK-8 reagent. The synergistic effect index Q (Q ≥ 1.15: synergistic effect) was obtained by the following formula, where E_{MMF}, E_{PTT} and E_{MPST} represent the respective treatment effects.

$$Q = \frac{E_{MIST}}{E_{MF} + (1 - E_{MMF})E_{PTT}} \quad (3)$$

4.11. Cell apoptosis analysis

The Annexin V-FITC Apoptosis Detection Kit was used to assess the apoptosis of MDA-MB-231 cells. Cells (2×10^5 pcs) were seeded in 6-well plates for 12 h to allow attachment according to the manufacturer's instructions. Next, MPCs (300 $\mu\text{g}/\text{mL}$) were treated in different ways after coinubation with cells for 12 h. Afterwards, cells were collected and washed twice with PBS through centrifugation at 1000g for 5 min, and then resuspended in binding buffer containing Annexin V-FITC and PI. After incubation in the dark for 15 min at room temperature, the cells were analyzed for apoptosis by flow cytometry (Fortessa, BD, America).

4.12. In vivo experiments of MDA-MB-231 breast cancer model

Female BALB/c mice (6–8 weeks old) were purchased from Nanjing Cavins Biotechnology Co., Ltd. (Nanjing, China) and used according to the protocol approved by the Regional Ethics Committee for Animal Experimentation of Ningbo University, China (license number: SYXK (Zhe) 2019-0005). A subcutaneous mouse model carrying triple-negative breast cancer MDA-MB-231 was established by injecting 8×10^6 MDA-MB-231 cells into the right abdomen of female nude mice. When the tumour volume reached 100 mm^3 , the mice were randomly divided into five groups ($n \geq 6$) including PBS, MPCs, MMF, PTT and MPST. Then, the MPCs were injected into the nude mice through the tail vein on day 0, day 3 and day 6, respectively. Next, the corresponding experiments were performed on different groups after 8 h of ingestion, where the treatment parameters for MMF and PTT were 60 mT, 1.5 Hz, 2 h and $1.5 \text{ W}/\text{cm}^2$, 15 min, respectively. The TUNEL staining was performed on the third day after treatment by randomly selecting one from each group. Additionally, body weight and tumour size were recorded every other day for 16 consecutive days. Then, the mice were sacrificed, and the organs and tumour tissues were collected and subjected to H&E staining and Prussian blue staining.

4.13. Statistical analysis

All data were statistically analyzed using the software GraphPad Prism 7. Data for each group are reported as mean \pm SD. For statistical significance, statistical analysis was performed using a *t*-test, * $p < 0.1$, ** $p < 0.01$, *** $p < 0.001$, **** $p < 0.0001$.

Credit author statement

Hui Du: Conceptualization, Methodology, Investigation, Data curation, Writing – original draft, Visualization, Validation. **Fang Yang:** Conceptualization, Supervision, Writing – review & editing, Validation, Funding acquisition. **Chenyang Yao:** Methodology, Investigation. **Wenhao Lv:** Methodology, Visualization, Validation. **Hao Peng:** Methodology, Validation. **Stefan G. Stanciu:** Conceptualization, Validation. **Harald A. Stenmark:** Writing – review & editing, Validation. **Young Min Song:** Writing – review & editing. **Bo Jiang:** Validation. **Aiguo Wu:** Conceptualization, Project administration, Resources, Supervision, Funding acquisition. Hui Du and Yang Fang contributed equally to this work.

Declaration of competing interest

The authors declare that they have no known competing financial interests or personal relationships that could have appeared to influence the work reported in this paper.

Data availability

The authors do not have permission to share data.

Acknowledgements

This work is supported by the National Natural Science Foundation of China (32025021, 31971292, 32111540257), the Youth Innovation Promotion Association, the Chinese Academy of Sciences (2022301), and the Ningbo 3315 Innovative Talent Project (2018-05-G). SGS and HAS acknowledge the support of the UEFISCDI grant RO-NO-2019-0601 MEDYCONAI. SGS, FY, and YMS acknowledge the support of the EsSENce CA19118 COST Action, which facilitated fruitful interactions.

Appendix A. Supplementary data

Supplementary data to this article can be found online at <https://doi.org/10.1016/j.biomaterials.2022.121868>.

References

- [1] G. Bianchini, J.M. Balko, I.A. Mayer, M.E. Sanders, L. Gianni, Triple-negative breast cancer: challenges and opportunities of a heterogeneous disease, *Nat. Rev. Clin. Oncol.* 13 (2016) 674–690.
- [2] W.D. Foulkes, I.E. Smith, J.S. Reis, Triple-negative breast cancer, *N. Engl. J. Med.* 363 (2010) 1938–1948.
- [3] T.H. Shin, J. Cheon, Synergism of nanomaterials with physical stimuli for biology and medicine, *Acc. Chem. Res.* 50 (2017) 567–572.
- [4] C. Wu, Y. Shen, M. Chen, K. Wang, Y. Li, Y. Cheng, Recent advances in magnetic-nanomaterial-based mechanotransduction for cell fate regulation, *Adv. Mater.* 30 (2018), e1705673.
- [5] D.J. Muller, J. Helenius, D. Alsteens, Y.F. Dufrene, Force probing surfaces of living cells to molecular resolution, *Nat. Chem. Biol.* 5 (2009) 383–390.
- [6] J.-w. Kim, H.-k. Jeong, K.M. Southard, Y.-w. Jun, J. Cheon, Magnetic nanotweezers for interrogating biological processes in space and time, *Acc. Chem. Res.* 51 (2018) 839–849.
- [7] M. Xie, W. Zhang, C. Fan, C. Wu, Q. Feng, J. Wu, Y. Li, R. Gao, Z. Li, Q. Wang, Y. Cheng, B. He, Bioinspired soft microrobots with precise magneto-collective control for microvascular thrombolysis, *Adv. Mater.* 32 (2020), e2000366.
- [8] R.J. Mannix, S. Kumar, F. Cassiola, M. Montoya-Zavala, E. Feinstein, M. Prentiss, D. E. Ingber, Nanomagnetic actuation of receptor-mediated signal transduction, *Nat. Nanotechnol.* 3 (2008) 36–40.
- [9] D. Seo, K.M. Southard, J.W. Kim, H.J. Lee, J. Farlow, J.U. Lee, D.B. Litt, T. Haas, A. P. Alivisatos, J. Cheon, Z.J. Gartner, Y.W. Jun, A mechanogenetic toolkit for interrogating cell signaling in space and time, *Cell* 165 (2016) 1507–1518.
- [10] J.U. Lee, W. Shin, Y. Lim, J. Kim, W.R. Kim, H. Kim, J.H. Lee, J. Cheon, Non-contact long-range magnetic stimulation of mechanosensitive ion channels in freely moving animals, *Nat. Mater.* 20 (2021) 1029–1036.
- [11] N. Wang, J.P. Butler, D.E. Ingber, Mechanotransduction across the cell surface and through the cytoskeleton, *Science* 260 (1993) 1124–1127.
- [12] A. Hillion, N. Hallali, P. Clerc, S. Lopez, Y. Lalatonne, C. Nous, L. Motte, V. Gigoux, J. Carrey, Real-time observation and analysis of magnetomechanical actuation of magnetic nanoparticles in cells, *Nano Lett.* 22 (2022) 1986–1991.
- [13] M.H. Cho, S. Kim, J.H. Lee, T.H. Shin, D. Yoo, J. Cheon, Magnetic tandem apoptosis for overcoming multidrug-resistant cancer, *Nano Lett.* 16 (2016) 7455–7460.
- [14] J. Wu, P. Ning, R. Gao, Q. Feng, Y. Shen, Y. Zhang, Y. Li, C. Xu, Y. Qin, G.R. Plaza, Q. Bai, X. Fan, Z. Li, Y. Han, M.S. Lesniak, H. Fan, Y. Cheng, Hedgehog-like gold-coated magnetic microspheres that strongly inhibit tumour growth through magnetomechanical force and photothermal effects, *Adv. Sci.* 7 (2020), 1902933.
- [15] Y. Chen, P. Han, Y. Wu, Z. Zhang, Y. Yue, W. Li, M. Chu, Programmable ROS-mediated cancer therapy via magneto-inductions, *Small* 14 (2018), e1802799.
- [16] Y. Ma, J. Xia, C. Yao, F. Yang, S.G. Stanciu, P. Li, Y. Jin, T. Chen, J. Zheng, G. Chen, H. Yang, L. Luo, A. Wu, Precisely tuning the contrast properties of $\text{Zn}_3\text{Fe}_{3-x}\text{O}_4$ nanoparticles in magnetic resonance imaging by controlling their doping content and size, *Chem. Mater.* 31 (2019) 7255–7264.
- [17] C. Yao, F. Yang, L. Sun, Y. Ma, S.G. Stanciu, Z. Li, C. Liu, O.U. Akakuru, L. Xu, N. Hampp, H. Lu, A. Wu, Magnetically switchable mechano-chemotherapy for enhancing the death of tumour cells by overcoming drug-resistance, *Nano Today* 35 (2020), 100967.
- [18] D. Peer, J.M. Karp, S. Hong, O.C. Farokhzad, R. Margalit, R. Langer, Nanocarriers as an emerging platform for cancer therapy, *Nat. Nanotechnol.* 2 (2007) 751–760.
- [19] L. Cheng, C. Wang, L. Feng, K. Yang, Z. Liu, Functional nanomaterials for phototherapies of cancer, *Chem. Rev.* 114 (2014) 10869–10939.
- [20] C. Xu, K. Pu, Second near-infrared photothermal materials for combinational nanotheranostics, *Chem. Soc. Rev.* 50 (2021) 1111–1137.
- [21] W. Tao, O.C. Farokhzad, Theranostic nanomedicine in the NIR-II window: classification, fabrication, and biomedical applications, *Chem. Rev.* 122 (2022) 5405–5407.

- [22] X. Li, J.F. Lovell, J. Yoon, X. Chen, Clinical development and potential of photothermal and photodynamic therapies for cancer, *Nat. Rev. Clin. Oncol.* 17 (2020) 657–674.
- [23] A. Chichet, J. Skowronek, M. Kubaszewska, M. Kanikowski, Hyperthermia – description of a method and a review of clinical applications, *Rep. Practical Oncol. Radiother.* 12 (2007) 267–275.
- [24] L.F. Fajardo, Pathological effects of hyperthermia in normal tissues, *Cancer Res.* 44 (1984) 4826–4835.
- [25] G.C. Li, N.F. Mivechi, G. Weitzel, Heat shock proteins, thermotolerance, and their relevance to clinical hyperthermia, *Int. J. Hyperther.* 11 (1995) 459–488.
- [26] H. Du, F. Yang, C. Yao, Z. Zhong, P. Jiang, S.G. Stanciu, H. Peng, J. Hu, B. Jiang, Z. Li, W. Lv, F. Zheng, H.A. Stenmark, A. Wu, Multifunctional modulation of high-performance Zn_xFe_{3-x}O₄ nanoparticles by precisely tuning the zinc doping content, *Small* 18 (2022), 2201669.
- [27] H. Chen, Y. Li, Y. Wang, P. Ning, Y. Shen, X. Wei, Q. Feng, Y. Liu, Z. Li, C. Xu, S. Huang, C. Deng, P. Wang, Y. Cheng, An engineered bacteria-hybrid microrobot with the magnetothermal bioswitch for remotely collective perception and imaging-guided cancer treatment, *ACS Nano* 16 (2022) 6118–6133.
- [28] Y.J. Jeong, J.S. Kang, S.I. Lee, D.M. So, J. Yun, J.Y. Baek, S.K. Kim, K. Lee, S. K. Park, Breast cancer cells evade paclitaxel-induced cell death by developing resistance to dasatinib, *Oncol. Lett.* 12 (2016) 2153–2158.
- [29] T. Paik, T.R. Gordon, A.M. Prantner, H. Yun, C.B. Murray, Designing tripodal and triangular gadolinium oxide nanoplates and self-assembled nanofibrils as potential multimodal bioimaging probes, *ACS Nano* 7 (2013) 2850–2859.
- [30] E.L. Elson, Cellular mechanics as an indicator of cytoskeletal structure and function, *Annu. Rev. Biophys.* 17 (1988) 397–430.
- [31] J.R. Lepock, Cellular effects of hyperthermia: relevance to the minimum dose for thermal damage, *Int. J. Hyperther.* 19 (2003) 252–266.
- [32] A. Ito, M. Fujioka, K. Tanaka, T. Kobayashi, H. Honda, Rinaldi, Screening of cytokines to enhance vaccine effects of heat shock protein 70-rich tumour cell lysate, *J. Biosci.* 100 (2005) 36–42.
- [33] M. Domenech, I. Marrero-Berrios, M. Torres-Lugo, C. Lysosomal membrane permeabilization by targeted magnetic nanoparticles in alternating magnetic fields, *ACS Nano* 7 (2013) 5091–5101.
- [34] E. Zhang, M.F. Kircher, M. Koch, L. Eliasson, S.N. Goldberg, E. Renstrom, Dynamic magnetic fields remote-control apoptosis via nanoparticle rotation, *ACS Nano* 8 (2014) 3192–3201.
- [35] J. Suzuki, D.P. Denning, E. Imanishi, H.R. Horvitz, S. Nagata, Xk-related protein 8 and CED-8 promote phosphatidylserine exposure in apoptotic cells, *Science* 341 (2013) 403–406.
- [36] J. Narula, E.R. Acio, N. Narula, L.E. Samuels, B. Fyfe, D. Wood, J.M. Fitzpatrick, P. N. Raghunath, J.E. Tomaszewski, C. Kelly, N. Steinmetz, A. Green, J.F. Tait, J. Leppo, F.G. Blankenberg, D. Jain, H.W. Strauss, Annexin-V imaging for noninvasive detection of cardiac allograft rejection, *Nat. Med.* 7 (2001) 1347–1352.
- [37] C. Wu, Y. Shen, M. Chen, K. Wang, C. Yu, Recent advances in magnetic-nanomaterial-based mechanotransduction for cell fate regulation, *Adv. Mater.* 30 (2018), 1705673.
- [38] Y.W. Pan, X.H. Ma, C. Liu, J. Xing, S.Q. Zhou, B. Parshad, T. Schwerdtle, W.Z. Li, A. G. Wu, R. Haag, Retinoic acid-loaded dendritic polyglycerol-conjugated gold nanostars for targeted photothermal therapy in breast cancer stem cells, *ACS Nano* 15 (2021) 15069–15084.